The Astrophysical Journal Letters, 912:L7 (9pp), 2021 May 1 https://doi.org/10.3847/2041-8213/abf64f

A Low-mass Cold and Quiescent Core Population in a Massive Star Protocluster

Shanghuo Li[1,2,3,4], Xing Lu[5], Qizhou Zhang[3], Chang Won Lee[1,6], Patricio Sanhueza[5,7], Henrik Beuther[8], Izaskun, Jiménez-Serra[9], Keping Qiu[10], Aina Palau[11], Siyi Feng[12,13,14], Thushara Pillai[15], Kee-Tae Kim[1,6], Hong-Li Liu[16], Josep Miquel. Girart[17], Tie Liu[2], Junzhi Wang[2], Ke Wang[18], Hauyu Baobab Liu[19], Howard A. Smith[3], Di Li[12,20], Jeong-Eun Lee[21], Fei Li[10], Juan Li[2], Shinyoung Kim[1,6], Nannan Yue[18], and Shaye Strom[3]

[1] Korea Astronomy and Space Science Institute, 776 Daedeokdae-ro, Yuseong-gu, Daejeon 34055, Republic of Korea; shanghuo.li@gmail.com
[2] Shanghai Astronomical Observatory, Chinese Academy of Sciences, 80 Nandan Road, Shanghai 200030, People's Republic of China
[3] Center for Astrophysics|Harvard & Smithsonian, 60 Garden Street, Cambridge, MA 02138, USA
[4] University of Chinese Academy of Sciences, 19A Yuquanlu, Beijing 100049, People's Republic of China
[5] National Astronomical Observatory of Japan, National Institutes of Natural Sciences, 2-21-1 Osawa, Mitaka, Tokyo 181-8588, Japan
[6] University of Science and Technology, 217 Gajeong-ro, Yuseong-gu, Daejeon 34113, Republic of Korea
[7] Department of Astronomical Science, SOKENDAI (The Graduate University for Advanced Studies), 2-21-1 Osawa, Mitaka, Tokyo 181-8588, Japan
[8] Max Planck Institute for Astronomy, Konigstuhl 17, D-69117 Heidelberg, Germany
[9] Centro de Astrobiología (CSIC-INTA), Ctra. de Torrejón a Ajalvir, Km. 4, Torrejón de Ardoz, E-28850 Madrid, Spain
[10] School of Astronomy and Space Science, Nanjing University, 163 Xianlin Avenue, Nanjing 210023, People's Republic of China
[11] Instituto de Radioastronomía y Astrofísica, Universidad Nacional Autónoma de México, P.O. Box 3-72, 58090, Morelia, Michoacán, México
[12] National Astronomical Observatories, Chinese Academy of Sciences, Beijing 100101, People's Republic of China
[13] Academia Sinica Institute of Astronomy and Astrophysics, No. 1, Sec. 4, Roosevelt Road, Taipei 10617, Taiwan
[14] National Astronomical Observatory of Japan, 2-21-1 Osawa, Mitaka, Tokyo, 181-8588, Japan
[15] Institute for Astrophysical Research, Boston University, 725 Commonwealth Avenue, Boston, MA 02215, USA
[16] Department of Astronomy, Yunnan University, Kunming, 650091, People's Republic of China
[17] Institut de Ciències de l'Espai (IEEC-CSIC), Campus UAB, Carrer de Can Magrans s/n, E-08193 Cerdanyola del Vallès, Catalonia, Spain
[18] Kavli Institute for Astronomy and Astrophysics, Peking University, 5 Yiheyuan Road, Haidian District, Beijing 100871, People's Republic of China
[19] Academia Sinica Institute of Astronomy and Astrophysics, 11F of AS/NTU Astronomy-Mathematics Building, No.1, Sec. 4, Roosevelt Road, Taipei 10617, Taiwan
[20] NAOC-UKZN Computational Astrophysics Centre, University of KwaZulu-Natal, Durban 4000, South Africa
[21] School of Space Research, Kyung Hee University, 1732, Deogyeong-Daero, Giheung-gu, Yongin-shi, Gyunggi-do 17104, Republic of Korea
Received 2021 March 16; revised 2021 April 6; accepted 2021 April 8; published 2021 April 29

Abstract

Pre-stellar cores represent the initial conditions of star formation. Although these initial conditions in nearby low-mass star-forming regions have been investigated in detail, such initial conditions remain vastly unexplored for massive star-forming regions. We report the detection of a cluster of low-mass starless and pre-stellar core candidates in a massive star protocluster-forming cloud, NGC 6334S. With the Atacama Large Millimeter/submillimeter Array (ALMA) observations at a ∼0.02 pc spatial resolution, we identified 17 low-mass starless core candidates that do not show any evidence of protostellar activity. These candidates present small velocity dispersions, high fractional abundances of NH_2D, high NH_3 deuterium fractionations, and are completely dark in the infrared wavelengths from 3.6 up to 70 μm. Turbulence is significantly dissipated and the gas kinematics are dominated by thermal motions toward these candidates. Nine out of the 17 cores are gravitationally bound, and therefore are identified as pre-stellar core candidates. The embedded cores of NGC 6334S show a wide diversity in masses and evolutionary stages.

Unified Astronomy Thesaurus concepts: Infrared dark clouds (787); Early-type stars (430); Star forming regions (1565); Star formation (1569); Interstellar medium (847); Interstellar line emission (844); Protoclusters (1297)

1. Introduction

Stars form in the high-density parts of molecular clouds, i.e., dense cores. A dense core prior to the protostellar phase is called a starless core, and a gravitationally bound/unstable starless core is referred to as a pre-stellar core (Ward-Thompson et al. 1994). The pre-stellar phase is considered to be the starting point in the star formation process (Bergin & Tafalla 2007; Caselli & Ceccarelli 2012). Pre-stellar cores can form single or multiple stellar systems under the combined effect of gravity, magnetic fields, and turbulence (Pineda et al. 2015). Understanding the properties of pre-stellar cores is critical for characterizing the initial conditions of cluster formation. The pre-stellar cores in low-mass star-forming regions near nearby molecular clouds, e.g., Perseus, Ophiuchus, Chamaeleon, Serpens, and Taurus (Lee et al. 1999, 2001; Enoch et al. 2008; Schnee et al. 2010; Dunham et al. 2016; Kirk et al. 2017; Tokuda et al. 2020) have been intensively studied. However, the studies of pre-stellar cores in massive cluster-forming regions are still limited by the low number of statistics available (Nony et al. 2018; Li et al. 2019; Sanhueza et al. 2019; Sahu et al. 2021).

The massive infrared dark cloud NGC 6334S (also known as IRDC G350.56+0.44) is located at the southwestern end of the NGC 6334 molecular cloud complex, which is a nearby (1.3 kpc; Chibueze et al. 2014) young and massive "mini-starburst" star-forming region (Willis et al. 2013). With a mass of $1.3 \times 10^3\ M_\odot$ (Li et al. 2020b), comparable to the clumps with embedded massive protostars and protoclusters in the complex, NGC 6334S has the potential to form a cluster encompassing both low- ($<2\ M_\odot$) and high-mass ($>8\ M_\odot$) stars. NGC 6334S provides an ideal laboratory to search for and study the early

stages (e.g., pre-stellar phase) of star formation in the high-mass regime.

In order to investigate massive star and cluster formation, we performed Atacama Large Millimeter/submillimeter Array (ALMA) and Karl G. Jansky Very Large Array (JVLA) observations of NGC 6334S. A study of 49 continuum dense cores (hereafter continuum cores) revealed by the 3 mm wavelength continuum image was presented in Li et al. (2020b), in which we reveal that the nonthermal motions are predominantly subsonic and transonic in both clump scale and continuum core scale. Here we use molecular lines to study the starless/pre-stellar cores.

2. Observations

2.1. ALMA Observations

We carried out a 55—pointing mosaic of NGC 6334S using the ALMA 12 m array in 2017 March (ID: 2016.1.00951.S). Two 234.4 MHz width spectral windows with a spectral resolution of 61 kHz ($\sim$0.21 km s^{-1} at 86 GHz) were configured to cover the $H^{13}CO^+$ (1–0, 86.754 GHz) and ortho-NH_2D (1_{11}–1_{01}, 85.926 GHz) lines, respectively. Three additional 1.875 GHz wide spectral windows at 88.5, 98.5, and 100.3 GHz with a coarse spectral resolution (3.0–3.3 km s^{-1}) were employed to obtain broad band continuum and rotational transitions of several molecular species (e.g., HCO^+ 1–0, HCN 1–0, CS 2–1, HNCO $4_{0,4}$–$3_{0,3}$, $H^{15}NC$ 1–0, CH_3OH $5_{1,4}$–$4_{1,3}$, SO 2_2–1_1, HC_3N 11–10). The maximum recoverable scales (MRSs) is $\sim$25″ in the ALMA data. The details of the observations can be found in Li et al. (2020b).

Data calibration and imaging were performed using CASA 4.7.0 (McMullin et al. 2007). We used Briggs' robust weighting of 0.5 to the visibilities for both the continuum and lines, which results in a synthesized beam of 3.″6 × 2.″4 with a position angle (PA) of 81° and 4.″1 × 2.″8 (PA = 83°) for continuum and line images, respectively. The achieved 1σ rms noise level is about 6 mJy beam^{-1} per 0.21 km s^{-1} for the line images and 30 μJy beam^{-1} for the continuum image. All images shown in this Letter are prior to primary beam correction, while all measured fluxes are corrected for the primary beam attenuation.

2.2. JVLA Observations

We carried out a 4-pointing mosaic of the central region of NGC 6334S using the JVLA C-configuration in 2014 August (ID:14A-241). The NH_3 (1, 1) through (5, 5) metastable inversion transitions and H_2O maser were simultaneously covered in this observation. CASA versions 4.7.0 and 5.1.1 were used to perform data calibration and imaging. An elliptical Gaussian with a FWHM of 6″ × 3″ (PA = 0°) was used to taper the visibilities, in order to increase the signal-to-noise ratio (S/N). This yields a synthesized beam size of about 10″ × 5″ (PA = 26°) with a 1σ rms noise of 9 mJy beam^{-1} per 0.2 km s^{-1} for the NH_3 lines. More details on the observations are presented in Li et al. (2020b).

3. Results and Analysis

3.1. Cold and Quiescent Cores

NH_2D (1_{11}–1_{01}, critical density $n_{cr} \sim 10^5$ cm^{-3}) is a good tracer of cold and dense molecular gas (Crapsi et al. 2007; Sanhueza et al. 2013), which can survive in the gas phase in the dense interior region of pre-stellar cores (Harju et al. 2017). In our ALMA data, the NH_2D (1_{11}–1_{01}) line emission is in general well correlated with the 3 mm continuum emission, but there are some exceptions: there are 17 bright compact structures in the NH_2D emission that are associated with weak (3σ–11σ) or no continuum emission (<3σ) at all (Figures 1 and 2), and with no young stellar object (YSO) counterparts (e.g., Class I/II; Willis et al. 2013). There is no reliable Class 0 catalog in this region. The details on the identification of NH_2D compact structures are summarized in Appendix A. We refer to these NH_2D compact structures as NH_2D cores, naming those in M1, M2, M3 ... in order of descending NH_2D velocity-integrated intensity. They have diameters ranging from 0.018 to 0.04 pc (see Table 1).

Among the NH_2D cores, M1 is the most prominent pre-stellar candidate with high S/N and a relatively isolated environment that eliminates the contamination from the outflows driven by the continuum cores. Therefore, the following analysis and discussion will use M1 as a showcase, while the physical parameters of the remaining NH_2D cores will only be included in statistical analyses.

Using the HCO^+, CS, HCN, SO, HNCO, and H_2O maser lines (see Figure 1), we have searched for signatures of protostellar activity, such as bipolar/monopolar/multipolar outflow activity and H_2O maser emission. All the NH_2D cores show no signs of protostellar activity. Although we currently cannot rule out the existence of unresolved or weak outflows due to the coarse spectral resolution and the lack of better low-mass outflow tracers such as CO, these NH_2D cores appear to be starless with the available evidence. In addition, the NH_2D cores do not show any appreciable (<3σ) continuum emission in the infrared wavelengths from 3.6 up to 70 μm, and therefore they are completely dark in these infrared images. The upper limit on the internal luminosity (L_{int}) of NH_2D cores is estimated to be $\sim$1.26 $L_\odot$ using Herschel/PACS 70 μm data (Tigé et al. 2017; see Appendix C for detailed derivation of internal luminosity). These results suggest that these NH_2D cores are cold and quiescent in terms of star-forming activity, though some undetected very faint embedded low-mass protostars cannot be fully ruled out (Dunham et al. 2008; Evans et al. 2009; Offner & McKee 2011; Fischer et al. 2017). An example of the comparison between NH_2D core (M1) and continuum core (#2) is shown in Figure 1, which includes all of the observed spectral windows. Continuum core #2 is a protostellar core as evidenced by the clear molecular outflows in the CS, HCN, and HCO^+ line emission, and it is one of the most chemically rich among the continuum cores. Nonetheless, only a few lines are detected toward continuum core #2. This indicates that the continuum cores #2 is at a stage prior to the hot cores/corinos. We note that M1 shows even less chemical complexity than continuum core #2, with fewer lines, molecular species, and narrower line profiles. This suggests that the evolutionary stages of the NH_2D cores are likely earlier than the continuum cores. On the other hand, we cannot completely rule out the possibility that some of continuum cores are relatively evolved pre-stellar cores, because of the lack of high sensitivity and high spectral resolution outflow tracers (e.g., CO, SiO) to distinguish the evolutionary stages (Li et al. 2020a). In this study, we will focus only on the NH_2D cores.

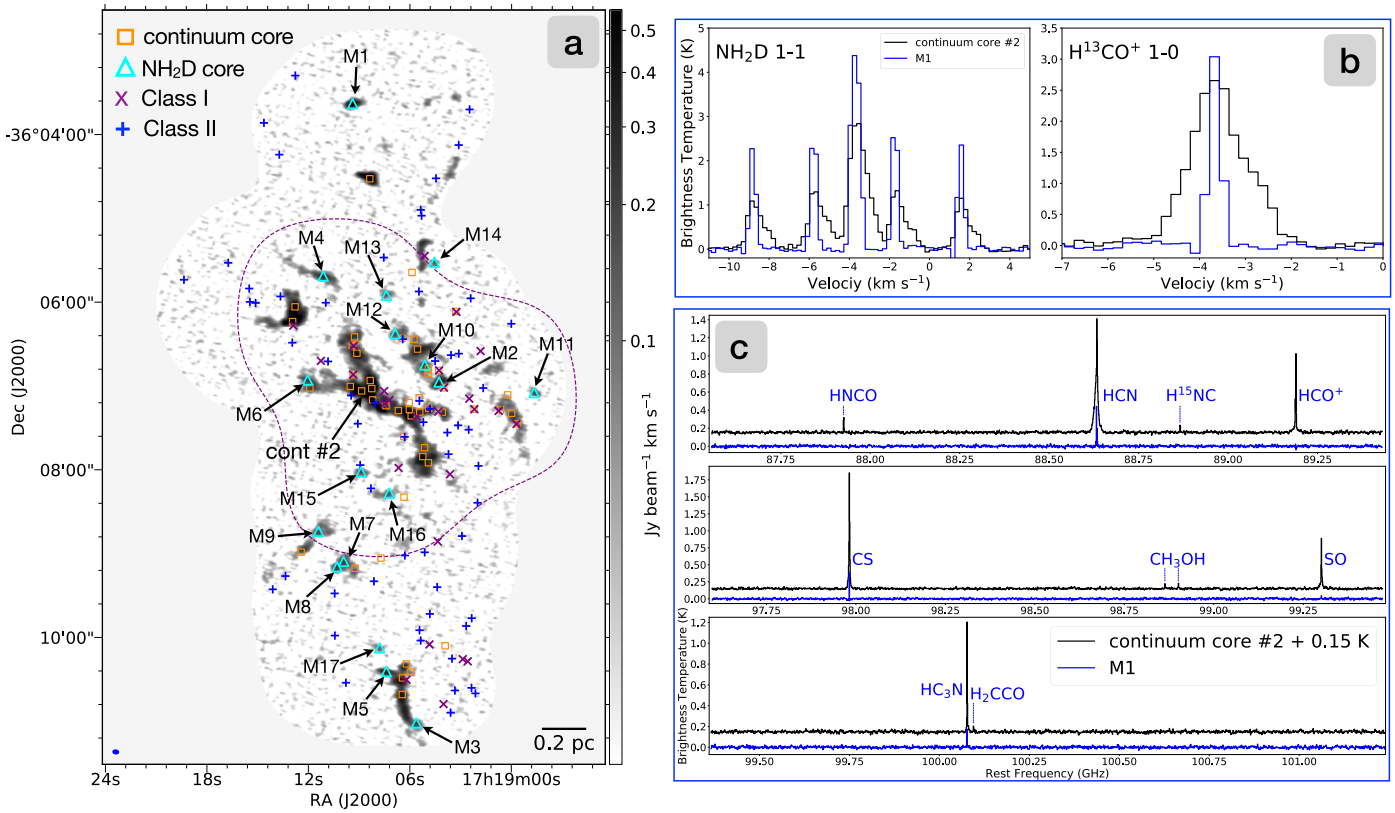

Figure 1. Panel a: the gray scale in the background shows the NH_2D velocity-integrated intensity (W_{NH_2D}) image. Cyan open triangles show the NH_2D cores. Yellow open squares present 49 continuum cores identified by ALMA 3 mm continuum image (Li et al. 2020b). Purple cross "x" and blue plus "+" symbols are 25 Class I and 58 Class II YSOs (Willis et al. 2013), respectively. The beam size of the NH_2D image is shown on the bottom left of the panel. The dashed purple contour shows the area mosaicked with the Very Large Array (VLA). Panel b: the core-averaged spectra of NH_2D (1_{11}–1_{01}) and $H^{13}CO^+$ (1–0) for continuum core #2 (black solid line) and NH_2D core M1 (blue solid line). Panel c: the core-averaged spectra of three wide (1.875 GHz) spectral windows for continuum core #2 (black solid line) and NH_2D core M1 (blue solid line), respectively.

3.2. Small Velocity Dispersions

The NH_2D line cube is fitted pixel by pixel, following the fitting processes described in Li et al. (2020b). In the hyperfine fits, the uncertainties of the centroid velocity and linewidths are small, while those of the excitation temperature and optical depth are relatively large (Figure 3). Figure 4 shows the observed velocity dispersions (σ_{obs}) distribution for each NH_2D core. All the NH_2D cores show small velocity dispersion ($\langle\sigma_{obs}\rangle \sim 0.16$ km s^{-1}) and the majority of them are smaller than the sound speed, $c_s(10\ K) = 0.19$ km s^{-1}. The observed velocity dispersions may be regarded as upper limits, given the limited spectral resolution, the blending of velocity components along the line of sight, and opacity-broadening effects. For the NH_2D cores, the linewidths of detected lines are smaller than those of the majority of continuum cores (see Figures 1 and 4).

Among all the NH_2D cores, M1 shows the strongest NH_2D emission and the smallest velocity dispersion. For M1, pixel by pixel fit to the NH_2D line cube yields a small mean velocity dispersion $\langle\sigma_{obs}\rangle \approx 0.107$ km s^{-1} (Figure 4), corresponding to an intrinsic observed velocity dispersion of $\sigma_{obs,int} = 0.06$ km s^{-1} after removing the smearing effect due to the channel width using $\sigma_{obs,int} = \sqrt{\sigma^2_{obs} - \sigma^2_{ch}}$, where $\sigma_{ch} = \triangle_{ch}/(2\sqrt{2\ln 2})^2 = 0.089$ km s^{-1} is the channel width. For the extremely narrow line emission, higher spectral resolution data is required to accurately characterize the actual intrinsic velocity dispersion. Considering the $\langle\sigma_{obs}\rangle$ is 1.2 times larger than the σ_{ch}, the aforementioned derived $\sigma_{obs,int}$ can be regarded as a reasonable approximation for the following analysis (see Appendix C in Li et al. 2020b). Assuming that the observed linewidths of the NH_2D line are caused only by thermal broadening, the gas temperature is found to be about 7 K, $\sigma_{th,NH_2D}(7\ K)$[22] $=\sigma_{obs,int} = 0.06$ km s^{-1}. This indicates that the gas kinematics is dominated by thermal motions with a kinetic temperature that is 7 K at most. In addition to M1, there are four NH_2D cores (M9, M12, M13, and M15) that also show extremely small velocity dispersions comparable to the NH_2D thermal velocity dispersion in the temperature range of 7–10 K. The velocity dispersions of remaining cores are relatively higher than the NH_2D thermal velocity dispersion at a temperature of 10 K ($\sigma_{th,\ NH_2D} \sim 0.07$ km s^{-1}), while they are much smaller than the sound speed (Figure 4). This indicates that the gas kinematics are dominated by thermal motions toward these NH_2D cores.

Figure 3 shows the annularly averaged observed velocity dispersion as a function of the radial distance (R_{dist}) from the center of M1. The observed velocity dispersion appears to increase with increasing R_{dist} (see Figure 3), which prevails in pre-stellar and starless cores (Crapsi et al. 2005; Auddy et al. 2019). The increase of σ_{obs} along R_{dist} is also detected in the other nine cores (M4, M6, M7, M8, M9, M10, M13, M15, M17), although the annularly averaged σ_{obs} starts to suffer

[22] The molecular thermal velocity dispersion can be calculated by $\sigma_{th} = \sqrt{(k_B T)/(\mu m_H)} = 9.08 \times 10^{-2}$ km s^{-1} $\left(\frac{T}{K}\right)^{0.5} \mu^{-0.5}$, where $\mu = m/m_H$ is the molecular weight, m is the molecular mass and m_H is the proton mass.

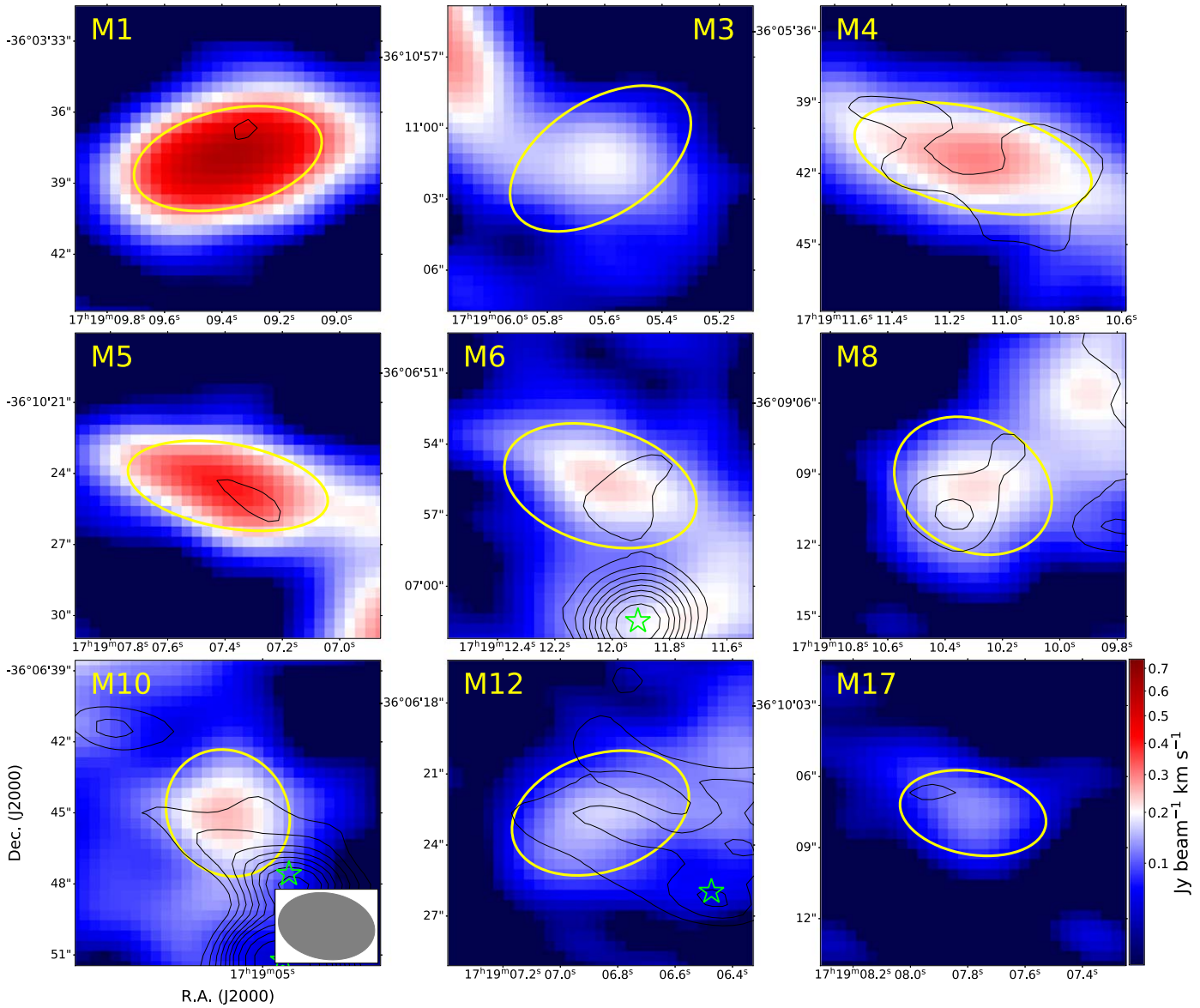

Figure 2. 3 mm continuum image (black contours) overlaid on the velocity-integrated intensity of NH_2D for the candidates that are gravitationally bound with $\alpha_{vir} < 2$. The integrated velocity range is -11.5 and 5.6 km s^{-1}. Black contours are (5, 7, 9, 11, 15, 17, 20, 24, 29) $\times \sigma$, where $\sigma = 30$ μJy beam^{-1} is the rms noise level of the continuum image. The yellow ellipses show the identified NH_2D cores. The green open stars indicate continuum cores. The beam size of NH_2D image is shown on the bottom right of M10 panel.

from low S/N toward the outer edges of the cores. This increasing trend of σ_{obs} along R_{dist} indicates that the turbulence is significantly dissipated toward the center of the core. The results indicate that the turbulence dissipation is commonly seen toward these NH_2D cores. Alternatively, in the larger-scale collapse scenario, if the pre-stellar cores undergo accretion, the infall speed decreases towards the center, and thus the line width will be smaller for more central regions (Gómez et al. 2021). Although no clear infall signatures are detected in M1 using coarser spectral resolution (3.0–3.3 km s^{-1}) optically thick lines (e.g., HCO^+ 1–0, HCN 1–0 and CS 2–1), this possibility cannot be ruled out and should be explored using higher spectral resolution data and other tracers (e.g., HCN 5–4/4–3/3–2 and HCO^+ 5–4/3–2; Chira et al. 2014).

Overall, the observed small velocity dispersions and their spatial distributions resemble those observed in the well-known pre-stellar cores in Ophiuchus/H-MM1 and L 1544 (Crapsi et al. 2007; Harju et al. 2017; Punanova et al. 2018). This suggests that the identified NH_2D cores may have not yet been affected by the star formation activities.

3.3. Gas Masses and Dynamical States

Assuming a typical temperature ($T_{dust} = 10$ K) of pre-stellar cores (see also Section 3.4), the gas masses (M_{gas}) of the NH_2D cores are estimated from continuum emission in two different approaches depending on their intensities (see Appendix B for a detailed derivation of gas mass). First, the continuum emission is used to compute the gas mass if the continuum peak emission is higher than 3σ. Second, a 3σ mass sensitivity of 0.13 $M_\odot$ is used as an upper limit for the core mass if the continuum peak emission is $\leqslant 3\sigma$. The derived cores masses are between $<$0.13 and 0.87 $M_\odot$, with a mean value of 0.45 $M_\odot$ (Table 1). Following the same procedure, the core-averaged H_2

Table 1
Physical Parameters of the NH_2D Cores

Core ID	R.A.	Decl.	Maj × Min	P.A.	R	σ_{obs}	v_{LSR}	$\mathcal{M}$	$W^{peak}_{NH_2D}$ (Jy/beam km/s)	W_{NH_2D} (Jy/beam km/s)	S^{peak}_{ν} (mJy beam^{-1})	S_{ν}	M_{gas}	M_{vir}	α_{vir}	N_{NH_2D}	N_{H_2}	$X(NH_2D)$	D_{NH_3}
	(J2000)	(J2000)	($''\times''$)	(deg)	(pc)	(km s^{-1})	(km s^{-1})					(mJy)	($M_{\odot}$)	($M_{\odot}$)		(cm^{-2})	(cm^{-2})		
(1)	(2)	(3)	(4)	(5)	(6)	(7)	(8)	(9)	(10)	(11)	(12)	(13)	(14)	(15)	(16)	(17)	(18)	(19)	(20)
M1	17:19:09.38	−36:03:37.96	7.1 × 2.8	107.6	0.028	0.11	−3.59	<0.68	0.69	140.95	0.174	0.294	0.43	<0.68	<1.57	2.2E+15	1.8E+22	1.1E-07	⋯
M2	17:19:04.28	−36:06:57.17	9.3 × 4.3	126.6	0.040	0.30	−1.36	2.41	0.40	136.13	0.186	0.412	0.61	2.54	4.18	6.1E+14	1.6E+22	3.2E-08	>0.39
M3	17:19:05.61	−36:11:01.29	7.5 × 3.9	75.4	0.034	0.20	−2.95	1.38	0.41	104.66	0.292	0.462	0.68	1.25	1.84	7.0E+14	2.4E+22	2.8E-08	⋯
M4	17:19:11.12	−36:05:41.37	9.4 × 3.2	79.5	0.034	0.17	−5.07	1.10	0.31	82.90	0.214	0.589	0.87	1.00	1.15	4.8E+14	2.8E+22	1.8E-08	0.25
M5	17:19:07.39	−36:10:24.52	7.5 × 2.1	72.1	0.025	0.15	−2.47	0.84	0.44	82.36	0.180	0.258	0.38	0.63	1.65	9.3E+14	1.8E+22	4.5E-08	⋯
M6	17:19:12.04	−36:06:55.76	7.3 × 3.9	57.3	0.034	0.18	−2.80	1.13	0.28	69.97	0.230	0.458	0.68	1.08	1.60	4.0E+14	2.4E+22	1.7E-08	>0.25
M7	17:19:09.91	−36:09:05.62	6.6 × 5.2	21.1	0.037	0.23	−4.17	1.69	0.23	65.62	0.206	0.447	0.66	1.83	2.77	1.8E+14	2.2E+22	8.0E-09	⋯
M8	17:19:10.30	−36:09:09.49	5.8 × 4.4	122.3	0.032	0.19	−4.22	1.32	0.24	56.76	0.237	0.450	0.66	1.27	1.91	3.0E+14	2.5E+22	1.2E-08	⋯
M9	17:19:11.40	−36:08:44.12	4.9 × 3.9	78.0	0.028	0.12	−1.68	0.34	0.24	45.38	0.158	0.201	0.30	0.73	2.47	2.7E+14	1.4E+22	1.4E-08	0.22
M10	17:19:05.12	−36:06:45.00	4.2 × 3.7	9.9	0.025	0.15	−3.47	0.78	0.26	45.19	0.310	0.366	0.54	0.79	1.46	6.9E+14	2.8E+22	2.5E-08	>0.11
M11	17:18:58.66	−36:07:04.76	4.1 × 2.2	48.5	0.019	0.11	−2.01	<0.73	0.33	44.30	⋯	⋯	<0.13	<0.51	3.82	7.5E+14	<1.5E+22	>7.1E-08	>0.32
M12	17:19:06.86	−36:06:22.65	6.8 × 3.6	124.3	0.031	0.13	−3.51	0.39	0.18	41.11	0.244	0.538	0.79	0.74	0.93	2.5E+14	3.0E+22	8.9E-09	>0.16
M13	17:19:07.39	−36:05:55.13	6.9 × 3.7	116.2	0.032	0.10	−5.36	<0.57	0.15	36.21	⋯	⋯	<0.13	<0.80	6.03	1.3E+14	<1.5E+22	>7.8E-09	>0.14
M14	17:19:04.55	−36:05:31.47	3.7 × 2.2	29.7	0.018	0.16	−4.20	0.93	0.26	33.59	⋯	⋯	<0.13	0.54	>4.04	2.8E+14	<1.5E+22	>1.2E-08	⋯
M15	17:19:08.88	−36:08:01.55	5.3 × 2.7	78.2	0.024	0.11	−4.26	<0.70	0.19	29.68	⋯	⋯	<0.13	<0.62	4.64	2.0E+14	<1.5E+22	>2.0E-08	>0.17
M16	17:19:07.21	−36:08:16.60	6.4 × 2.3	125.7	0.024	0.15	−4.18	0.81	0.16	29.59	0.160	0.168	0.25	0.60	2.44	1.6E+14	1.2E+22	1.1E-08	>0.14
M17	17:19:07.78	−36:10:07.54	4.8 × 1.8	57.5	0.019	0.13	−2.52	0.49	0.13	18.00	0.158	0.170	0.25	0.43	1.70	1.6E+14	1.6E+22	7.2E-09	⋯
Mean					0.028	0.16		0.96	0.29	62.50	0.211	0.370	0.45	0.94	2.60	5.1E+14	2.0E+22	2.6E-08	0.22
Median					0.028	0.15		0.81	0.26	45.38	0.206	0.412	0.43	0.74	1.91	3.0E+14	1.8E+22	1.7E-08	0.20
Minimum					0.018	0.10		0.34	0.13	18.00	0.158	0.168	0.13	0.43	0.93	1.3E+14	1.2E+22	7.2E-09	0.11
Maximum					0.040	0.30		2.41	0.69	140.95	0.310	0.589	0.87	2.54	6.03	2.2E+15	3.0E+22	1.1E-07	0.39

Notes. For M1, M11, M13, and M15, $\sigma_{nt,NH_2D} = \sigma_{obs}$ was used as the $\sigma_{obs,int} \leqslant \sigma_{nt,NH_2D}(10K)$. (4)–(5) Beam-deconvolved size. (6) Beam-deconvolved effective radius. (7)–(8) σ_{obs} and v_{LSR} are derived by the core-averaged spectrum. (9) Mach number $\mathcal{M} = \sqrt{3}\,\sigma_{nt,NH_2D}/c_s$. (10) The peak value of NH_2D velocity-integrated image. (11) The integrated flux density of the NH_2D line emission. (12)–(13) The peak and integrated intensity of continuum emission. (14) Gas mass estimated by continuum emission. (15) Virial mass. (16) Virial parameter. (17) Mean NH_2D column density. (18) Mean H_2 column density. (19) Mean NH_2D abundance fraction. (20) The NH_3 deuterium fractionation D_{NH_3}.

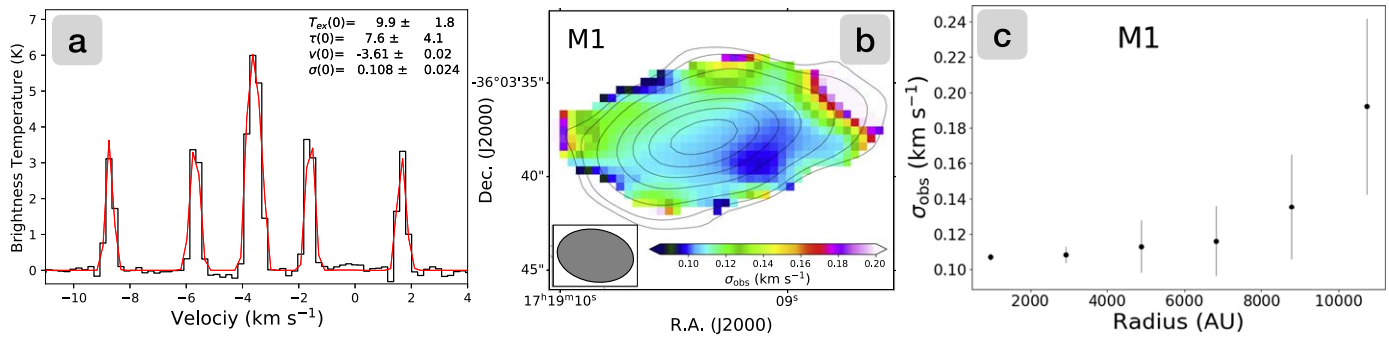

Figure 3. Panel a: NH_2D spectrum (black curve) extracted from single pixels toward M1. Red curve shows the best result from the hyperfine fitting that includes NH_2D 36 hyperfine components (Ginsburg & Mirocha 2011; Daniel et al. 2016), with the best-fit parameters displayed in the panel. Panel b: the NH_2D integrated intensity (black contours) overlaid on its σ_{obs} toward M1. The contours are (3, 5, 10, 20, 30, 40, 50) × σ, with $\sigma = 0.011$ Jy beam^{-1} km s^{-1}. The beam size is shown on the lower left of the panel. Panel c: the annularly averaged observed velocity dispersions (σ_{obs}) as a functions of radial distance from the center (given in Table 1) of M1. The error bars show the statistical standard deviation at each bin.

column densities (N_{H_2}) are derived to be between $<1.1 \times 10^{22}$ and 3.0×10^{22} cm^{-2} (Appendix B), with a mean value of 2.0×10^{22} cm^{-2}.

In order to evaluate the gravitational bound of the NH_2D cores, we estimated the virial masses (M_{vir}) that range from 0.43 to 2.54 $M_\odot$ (see Appendix B for a derivation of virial mass). The derived virial parameters, $\alpha_{vir} = M_{vir}/M_{gas}$, are between 0.93 and 6.03. Nine out of the 17 NH_2D cores are gravitationally bound with virial parameters <2, and the remaining eight NH_2D cores are gravitationally unbound with $\alpha_{vir} > 2$ if external pressure is ignored (Kauffmann et al. 2013).

3.4. NH_2D Abundances and NH_3 Deuterium Fractionation

Assuming a constant temperature of 10 K and the ortho-to-para ratio of 3 (Harju et al. 2017), the estimated NH_2D column densities ($N(NH_2D)$) range from 7.3×10^{12} cm^{-2} to 3.4×10^{15} cm^{-2}, with a mean value of 5.2×10^{14} cm^{-2} (see Figure 4). The derived abundance $X(NH_2D) = N(NH_2D)/N(H_2)$ toward the NH_2D cores range from 1.8×10^{-9} to 2.0×10^{-7}, with a mean value of 2.5×10^{-8}.

The JVLA NH_3 observations only cover the central region of NGC 6334S (see Figure 1). There are 10 NH_2D cores located in the field of the NH_3 observations. Limited by the relatively low S/N, both NH_3 (1,1) and (2,2) transitions are detected in M4 and M10 (S/N ∼ 4–5), while only NH_3 (1,1) is marginally detected in M13 and undetected in the other seven NH_2D cores. Using `PySpecKit` we fit the core-averaged spectrum, and we derive a kinetic temperature of $T_k = 12.7 \pm 3.1$ K and a column density of $N_{NH_3} = (4.4 \pm 2.5) \times 10^{14}$ cm^{-2} for M4, and the derived parameters are $T_k = 12.1 \pm 3.2$ K and $N_{NH_3} = (8.9 \pm 5.0) \times 10^{14}$ cm^{-2} for M10, assuming the ortho-to-para ratio of 1 for NH_3 (Harju et al. 2017). The column density ratio NH_2D-to-NH_3 (D_{NH_3}, also known as NH_3 deuterium fractionation) is found to be 0.25 and 0.11 for M4 and M10, respectively. A 3σ integrated intensity is used to estimate the upper limit column density (3.8×10^{14} cm^{-2}) for the other eight cores assuming an excitation temperature of 10 K. The resulting lower limits D_{NH_3} range from 0.11 to 0.39 (see Table 1), which are close to those in the pre-stellar core L 1544 (0.5 ± 0.2; Crapsi et al. 2007) and Ophiuchus/H-MM1 (0.45 ± 0.09; Harju et al. 2017).

4. Discussion

As shown in Figure 4, the derived NH_2D column densities and fractional abundances are higher than the values of Ophiuchus/H-MM1 (1.1×10^{14} cm^{-2} and 2×10^{-9}; Harju et al. 2017) and L1544 (1.8×10^{14} cm^{-2} and 2×10^{-10}; Crapsi et al. 2007). The high abundances of NH_2D could benefit from the significant depletion of CO, which occurs faster at cold and dense environments (e.g., starless or pre-stellar cores; the detail chemical processes related to the NH_2D formation can be found in Sipilä et al. 2015; Harju et al. 2017).

The small velocity dispersion, small Mach number (Table 1), and positive σ_{obs}–R_{dist} relation indicate that the turbulence is likely dissipated toward these NH_2D cores. In addition, it implies that star formation has not yet started; outflows motions would widen the lines as can be seen in the continuum cores (Figure 1). Therefore, these results, in conjunction with the high NH_3 deuterium fractionation and the lack of embedded YSOs and 70 μm emission, indicate that the identified NH_2D cores are still in a starless phase. Nine out of 17 starless cores are gravitationally bound with $\alpha_{vir} < 2$; therefore, they are identified as excellent pre-stellar core candidates. The dust temperature may drop to ∼5.5 K toward the core center (e.g., L1544; Crapsi et al. 2007). The derived gas mass can increase by a factor of 2.25 if a temperature of 5.5 K is assumed, so that the resulting virial parameter will decrease by a factor of 2.25. The levels of the missing flux are unknown due to the lack of single dish data. However, the estimated masses and radius of cores may not be significantly affected by the missing flux, because the observations are carried out with the most compact 12 m array configuration (C40-1) and the MRS is ∼25″, which is much larger than the cores sizes. Therefore, the estimated virial parameters are not seriously affected by the missing flux. In addition, the ambient pressure from the parental clumps and filaments could also provide additional confinement to make these NH_2D cores bound (e.g., Chen et al. 2019; Li et al. 2020b). Therefore, we cannot completely rule out the possibility that the other eight starless cores could also be pre-stellar core candidates.

The estimated masses of NH_2D cores range from 0.13 to 0.87 $M_\odot$, suggesting that they are in the low-mass core regime. The majority (15) of NH_2D cores are associated with filamentary structures revealed by the $H^{13}CO^+$ line emission (S. Li et al. 2021, in preparation). Therefore, the NH_2D cores

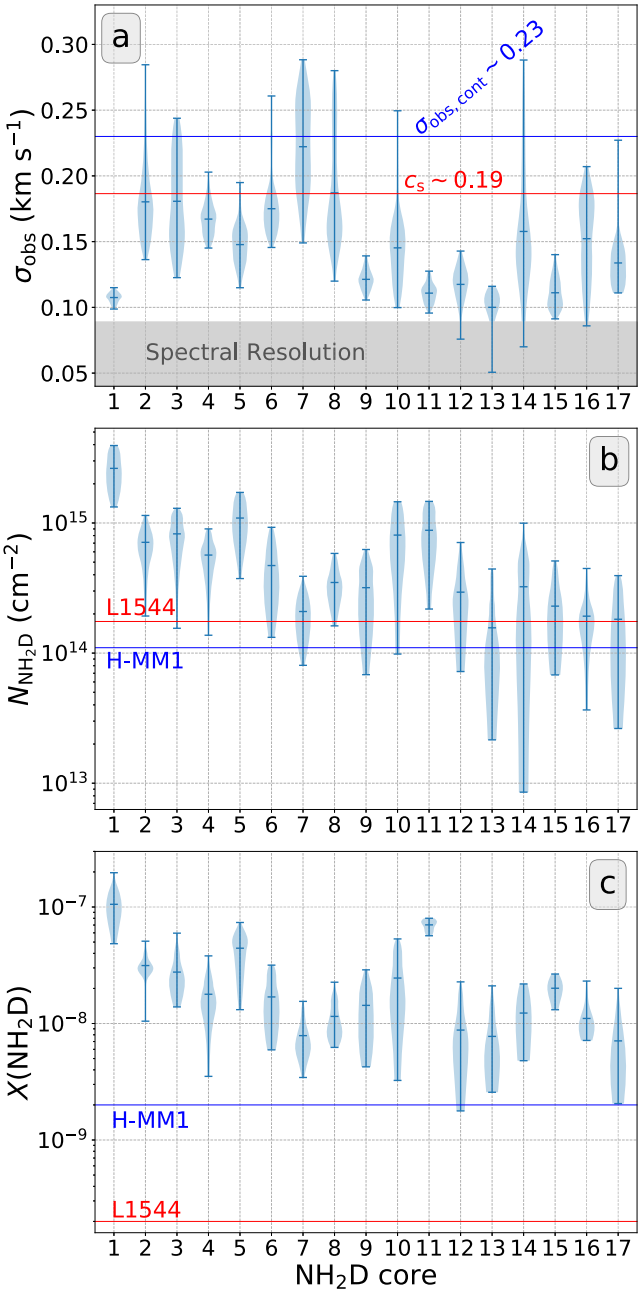

Figure 4. Panels a to c: violin plots of the σ_{obs}, N_{NH_2D}, and $\chi(NH_2D)$ distributions for all NH_2D cores. The shape of each distribution shows the probability density of the data smoothed by a kernel density estimator. The blue bars from the top to bottom represent the maximum, mean, and minimum values, respectively. Panel a: the red solid line is the sound speed at a temperature of 10 K. The blue solid line is the mean observed velocity dispersion of the continuum cores, $\langle\sigma_{obs,cont}\rangle = 0.23 \pm 0.08$ km s^{-1}. The shaded gray region shows the spectral resolution limit of the NH_2D line. Panel b: the red and blue solid lines are observed $N(NH_2D)$ in the pre-stellar core L1544 (1.75×10^{14} cm^{-2}; Crapsi et al. 2007) and Ophiuchus/H-MM1 (1.1×10^{14} cm^{-2}; Harju et al. 2017). Panel c: the blue and red solid lines are observed abundance $X(NH_2D)$ in the pre-stellar cores Ophiuchus/H-MM1 (2×10^{-9}, Harju et al. 2017) and L1544 (2×10^{-10}, Crapsi et al. 2007), respectively.

have the potential to accrete a significant amount of material from the parental clump via filamentary accretion. The masses of continuum cores are found to range from low- to high-mass regime (0.17–14.03 $M_\odot$; Li et al. 2020b). These results suggest that cores with a large range of masses are simultaneously forming in this cluster-forming cloud. The massive cores are found toward the center of cloud (see Li et al. 2020b), while the low-mass cores are wide spread throughout the region. The evolutionary stages vary significantly over the sample of NH_2D cores, continuum cores, and YSOs (Class I and II). This indicates that there is a temporally continuous formation of low- to high-mass cores.

In summary, NGC 6334S is forming a stellar protocluster, its embedded cores show a wide diversity in masses (0.13–14.03 $M_\odot$) and evolutionary stages (pre-stellar–Class II phases), and the embedded cores are expected to grow in mass by gas accretion from parental clump via filaments. This seems to be consistent with the competitive accretion massive star formation scenario (Bonnell & Bate 2006), in which the dense cores located near the center of the gravitational potential continue accreting material to form massive stars.

5. Summary

We present ALMA and JVLA high spatial resolution observations toward the massive IRDC NGC 6334S. We have identified 17 low-mass starless core candidates that show bright NH_2D emission, but no YSO counterparts and no signs of protostellar activity, although we cannot completely rule out the possibility of very weak (and thus undetected) outflows or very faint embedded low-mass protostars. These candidates show almost-thermal velocity dispersions (down to $\sigma_{tot} \sim 0.06$ km s^{-1}), high NH_2D abundances (up to $\sim 10^{-7}$), high NH_3 deuterium fractionations (up to >0.39), and are completely dark in the infrared wavelengths from 3.6 up to 70 μm. In addition, the σ_{obs} appear to decrease toward the center of cores in 10 of them. These results suggest that turbulence has significantly dissipated and the NH_2D abundance has significantly enhanced toward these cores. The gas kinematics resemble the well-known pre-stellar cores, e.g., Ophiuchus/H-MM1 and L 1544, but with one to two orders of magnitude greater NH_2D abundance (Crapsi et al. 2007; Harju et al. 2017). Nine out of the 17 NH_2D cores are gravitationally bound, and therefore are identified as pre-stellar core candidates. Therefore, the NH_2D line could be a powerful tracer to reveal the starless and pre-stellar cores that do not show significant dust continuum emission. This is the first detection of a cluster of low-mass starless and pre-stellar core candidates in a massive star cluster-forming cloud. Low- to high-mass cores are simultaneously forming in this cluster-forming cloud.

We thank the anonymous referee for constructive comments that helped improve this Letter. This work was partially supported by National Natural Science Foundation of China (NSFC, grant Nos. 11988101, 11911530226). C.W.L. is supported by the Basic Science Research Program through the National Research Foundation of Korea (NRF) funded by the Ministry of Education, Science and Technology (NRF-2019R1A2C1010851). H.B. acknowledges support from the European Research Council under the European Community's Horizon 2020 framework program (2014-2020) via the ERC Consolidator Grant "From Cloud to Star Formation (CSF)" (project number 648505). H.B. also acknowledges funding from the Deutsche Forschungsgemeinschaft (DFG) via the Collaborative Research Center (SFB 881) "The Milky Way System" (subproject B1). I.J.-S. has received partial support from the Spanish State Research Agency (AEI; project number PID2019-105552RB-C41). K.Q. is partially supported by

National Key R&D Program of China No. 2017YFA0402600, and acknowledges the National Natural Science Foundation of China (NSFC) grant U1731237. A.P. acknowledges financial support from the UNAM-PAPIIT IN111421 grant, the Sistema Nacional de Investigadores of CONACyT, and from the CONACyT project number 86372 of the "Ciencia de Frontera 2019" program, entitled "Citlalcóatl: A multiscale study at the new frontier of the formation and early evolution of stars and planetary systems," México. J.M.G. acknowledges the support of the grant AYA2017-84390-C2-R (AEI/FEDER, EU). K.W. acknowledges support by the National Key Research and Development Program of China (2017YFA0402702, 2019YFA0405100), the National Science Foundation of China (11973013, 11721303), NSFC grant 11629302, and the starting grant at the Kavli Institute for Astronomy and Astrophysics, Peking University (7101502287). H.B.L. is supported by the Ministry of Science and Technology (MoST) of Taiwan (grant Nos. 108-2112-M-001-002-MY3). This Letter makes use of the following ALMA data: ADS/JAO.ALMA#2016.1.00951.S. ALMA is a partnership of ESO (representing its member states), NSF (USA) and NINS (Japan), together with NRC (Canada), MOST and ASIAA (Taiwan), and KASI (Republic of Korea), in cooperation with the Republic of Chile. The Joint ALMA Observatory is operated by ESO, AUI/NRAO and NAOJ.

Facilities: ALMA, JVLA, Herschel.

Software: CASA (McMullin et al. 2007), APLpy (Robitaille & Bressert 2012), Astropy (Astropy Collaborationet al. 2013), Matplotlib (Hunter 2007), PySpecKit (Ginsburg & Mirocha 2011).

Appendix A
NH_2D Core Identification

The `astrodendro`[23] algorithm was used to preselect the compact NH_2D emission structures (i.e., the leaves in the terminology of `astrodendro`; Rosolowsky et al. 2008) from the NH_2D velocity-integrated intensity image (integrated between -11.5 and 5.6 km s^{-1}). The following parameters are used in the computation of `astrodendro`: the minimum pixel value is 3σ noise level ($1\sigma \sim 0.02$ Jy beam^{-1} km s^{-1} for W_{NH_2D}); the peak value is $\geqslant 6\sigma$; the minimum difference in the peak intensity between neighboring compact structures is 1σ; and the minimum number of pixels required for a structure to be considered an independent entity is 40 (approximately the synthesized beam area). From the identified leaves, we further search for the compact structures that are not associated with continuum cores, YSOs, and show a single peak and no extreme elongations (the major axis being smaller than 3 times the minor axis). The physical parameters (size, flux density, and peak intensity) of these selected compact structures are extracted from the NH_2D velocity-integrated intensity image using the `CASA-imfit` task (see Table 1). We stress that this identification is likely to be incomplete. Potential NH_2D compact structures could have been missed if they cannot be distinguished from the clumpy or filamentary structures. Four NH_2D cores (M11, M13, M14, M15) are not associated with continuum emission at all ($<3\sigma$, $1\sigma \sim 30$ μJy beam^{-1} for continuum image), and the rest of the NH_2D cores are partially associated with weak continuum emission (3σ–7σ), except for M10 that has about 10% region at the edge of the core associated with 8σ–11σ continuum emission (Figure 2).

[23] http://dendrograms.org/

Appendix B
Gas Mass and Virial Mass

With the observed 3 mm continuum fluxes, we estimated the gas mass (M_{gas}) of identified cores assuming optically thin modified black body emission in the Rayleigh–Jeans limit, following

$$M_{gas} = \eta \frac{S_\nu d^2}{B_\nu(T)\kappa_\nu}, \tag{B1}$$

where $\eta = 100$ is the assumed gas-to-dust mass ratio, d is the source distance, S_ν is the continuum flux at frequency 98.5 GHz, $B_\nu(T)$ is the Planck function at temperature T, and κ_ν is the dust opacity at frequency ν. We adopt $\kappa_{98.5\ \mathrm{GHz}} = 0.235\ \mathrm{cm^2 g^{-1}}$, assuming $\kappa_\nu = 10(\nu/1.2\ \mathrm{THz})^\beta\ \mathrm{cm^2\ g^{-1}}$ and $\beta = 1.5$ for all of dense cores (Hildebrand 1983).

The column density (N_{H_2}) is computed with

$$N_{H_2} = \eta \frac{S_\nu^{beam}}{B_\nu(T)\kappa_\nu\ \Omega\ \mu\ m_H}, \tag{B2}$$

where S_ν^{beam} is the continuum flux density, Ω is the beam solid angle, $\mu = 2.8$ is the mean molecular weight of the interstellar medium (Kauffmann et al. 2008), and m_H is the proton mass.

The virial mass is estimated using

$$M_{vir} = \frac{5}{a\beta}\frac{\sigma_{tot}^2 R}{G}, \tag{B3}$$

where $\sigma_{tot} = \sqrt{\sigma_{nt,NH_2D}^2 + \sigma_{th,\langle m\rangle}^2}$ $= \sqrt{(\sigma_{obs,int}^2 - \sigma_{th,NH_2D}^2) + \sigma_{th,\langle m\rangle}^2}$ is the total velocity dispersion, R is the effective radius, G is the gravitational constant, parameter a equals to $(1-b/3)/(1-2b/5)$ for a power-law density profile $\rho \propto r^{-b}$, and $\beta = (\arcsin e)/e$ is the geometry factor (see also Li et al. 2013, 2020b). Here $\langle m\rangle$ is $2.37 m_H$ (Kauffmann et al. 2008), $\sigma_{obs,int}$ is derived by the core-averaged spectrum, and b is assumed to be 2. For M1, M11, M13, and M15, $\sigma_{tot} = \sigma_{th,\langle m\rangle}(10\ \mathrm{K})$ was used as the $\sigma_{obs,int} \leqslant \sigma_{th,NH_2D}(10\ \mathrm{K})$.

Appendix C
Internal Luminosity

The internal luminosity of dense object can be estimated by using the empirical relationship between internal luminosity (L_{int}) and observed 70 μm flux (Dunham et al. 2008):

$$L_{int}(L_\odot) = 3.3 \times 10^8 \left(F_{70}\left(\frac{d}{140\ \mathrm{pc}}\right)^2\right)^{0.94}, \tag{C1}$$

where F_{70} is the flux at 70 μm in cgs units (erg s^{-1} cm^{-2} Hz^{-1}) and d is the source distance in pc. A 3σ sensitivity of $\sim$0.3 Jy from `Herschel`/PACS 70 μm observation is used to derived an upper limit ($\sim 1.26\ L_\odot$) of internal luminosity for the identified NH_2D cores (Tigé et al. 2017), with the exception of M3, M5, and M17, which are illuminated by the western YSOs

rather than internal heating. The measured 70 μm fluxes of M3, M5, and M7 are about 5–6σ.

ORCID iDs

Shanghuo Li https://orcid.org/0000-0003-1275-5251
Xing Lu https://orcid.org/0000-0003-2619-9305
Qizhou Zhang https://orcid.org/0000-0003-2384-6589
Chang Won Lee https://orcid.org/0000-0002-3179-6334
Patricio Sanhueza https://orcid.org/0000-0002-7125-7685
Henrik Beuther https://orcid.org/0000-0002-1700-090X
Izaskun, Jiménez-Serra https://orcid.org/0000-0003-4493-8714
Keping Qiu https://orcid.org/0000-0002-5093-5088
Aina Palau https://orcid.org/0000-0002-9569-9234
Siyi Feng https://orcid.org/0000-0002-4707-8409
Thushara Pillai https://orcid.org/0000-0003-2133-4862
Kee-Tae Kim https://orcid.org/0000-0003-2412-7092
Hong-Li Liu https://orcid.org/0000-0003-3343-9645
Josep Miquel. Girart https://orcid.org/0000-0002-3829-5591
Tie Liu https://orcid.org/0000-0002-5286-2564
Junzhi Wang https://orcid.org/0000-0001-6106-1171
Ke Wang https://orcid.org/0000-0002-7237-3856
Hauyu Baobab Liu https://orcid.org/0000-0003-2300-2626
Di Li https://orcid.org/0000-0003-3010-7661
Jeong-Eun Lee https://orcid.org/0000-0003-3119-2087
Fei Li https://orcid.org/0000-0002-9832-8295
Juan Li https://orcid.org/0000-0003-3520-6191
Shinyoung Kim https://orcid.org/0000-0001-9333-5608
Nannan Yue https://orcid.org/0000-0003-0355-6875

References

Astropy Collaboration, Robitaille, T. P., Tollerud, E. J., et al. 2013, A&A, 558, A33
Auddy, S., Myers, P. C., Basu, S., et al. 2019, ApJ, 872, 207
Bergin, E. A., & Tafalla, M. 2007, ARA&A, 45, 339
Bonnell, I. A., & Bate, M. R. 2006, MNRAS, 370, 488
Caselli, P., & Ceccarelli, C. 2012, A&ARv, 20, 56
Chen, H. H.-H., Pineda, J. E., Goodman, A. A., et al. 2019, ApJ, 877, 93
Chibueze, J. O., Omodaka, T., Handa, T., et al. 2014, ApJ, 784, 114
Chira, R.-A., Smith, R. J., Klessen, R. S., Stutz, A. M., & Shetty, R. 2014, MNRAS, 444, 874
Crapsi, A., Caselli, P., Walmsley, C. M., et al. 2005, ApJ, 619, 379
Crapsi, A., Caselli, P., Walmsley, M. C., & Tafalla, M. 2007, A&A, 470, 221
Daniel, F., Coudert, L. H., Punanova, A., et al. 2016, A&A, 586, L4
Dunham, M. M., Crapsi, A., Evans, N. J. I., et al. 2008, ApJS, 179, 249
Dunham, M. M., Offner, S. S. R., Pineda, J. E., et al. 2016, ApJ, 823, 160
Enoch, M. L., Evans, N. J. I., Sargent, A. I., et al. 2008, ApJ, 684, 1240
Evans, N. J. I., Dunham, M. M., Jørgensen, J. K., et al. 2009, ApJS, 181, 321
Fischer, W. J., Megeath, S. T., Furlan, E., et al. 2017, ApJ, 840, 69
Ginsburg, A., & Mirocha, J. 2011, PySpecKit: Python Spectroscopic Toolkit, Astrophysics Source Code Library, ascl:1109.001
Gómez, G. C., Vázquez-Semadeni, E., & Palau, A. 2021, MNRAS, 502, 4963
Harju, J., Daniel, F., Sipilä, O., et al. 2017, A&A, 600, A61
Hildebrand, R. H. 1983, QJRAS, 24, 267
Hunter, J. D. 2007, CSE, 9, 90
Kauffmann, J., Bertoldi, F., Bourke, T. L., Evans, N. J. I., & Lee, C. W. 2008, A&A, 487, 993
Kauffmann, J., Pillai, T., & Goldsmith, P. F. 2013, ApJ, 779, 185
Kirk, H., Dunham, M. M., Di Francesco, J., et al. 2017, ApJ, 838, 114
Lee, C. W., Myers, P. C., & Tafalla, M. 1999, ApJ, 526, 788
Lee, C. W., Myers, P. C., & Tafalla, M. 2001, ApJS, 136, 703
Li, D., Kauffmann, J., Zhang, Q., & Chen, W. 2013, ApJL, 768, L5
Li, S., Sanhueza, P., Zhang, Q., et al. 2020a, ApJ, 903, 119
Li, S., Zhang, Q., Liu, H. B., et al. 2020b, ApJ, 896, 110
Li, S., Zhang, Q., Pillai, T., et al. 2019, ApJ, 886, 130
McMullin, J. P., Waters, B., Schiebel, D., Young, W., & Golap, K. 2007, in ASP Conf. Ser. 376, Astronomical Data Analysis Software and Systems XVI, ed. R. A. Shaw, F. Hill, & D. J. Bell (San Francisco, CA: ASP), 127
Nony, T., Louvet, F., Motte, F., et al. 2018, A&A, 618, L5
Offner, S. S. R., & McKee, C. F. 2011, ApJ, 736, 53
Pineda, J. E., Offner, S. S. R., Parker, R. J., et al. 2015, Natur, 518, 213
Punanova, A., Caselli, P., Feng, S., et al. 2018, ApJ, 855, 112
Robitaille, T., & Bressert, E. 2012, APLpy: Astronomical Plotting Library in Python, Astrophysics Source Code Library, ascl:1208.017
Rosolowsky, E. W., Pineda, J. E., Kauffmann, J., & Goodman, A. A. 2008, ApJ, 679, 1338
Sahu, D., Liu, S.-Y., Liu, T., et al. 2021, ApJL, 907, L15
Sanhueza, P., Contreras, Y., Wu, B., et al. 2019, ApJ, 886, 102
Sanhueza, P., Jackson, J. M., Foster, J. B., et al. 2013, ApJ, 773, 123
Schnee, S., Enoch, M., Johnstone, D., et al. 2010, ApJ, 718, 306
Sipilä, O., Harju, J., Caselli, P., & Schlemmer, S. 2015, A&A, 581, A122
Tigé, J., Motte, F., Russeil, D., et al. 2017, A&A, 602, A77
Tokuda, K., Fujishiro, K., Tachihara, K., et al. 2020, ApJ, 899, 10
Ward-Thompson, D., Scott, P. F., Hills, R. E., & Andre, P. 1994, MNRAS, 268, 276
Willis, S., Marengo, M., Allen, L., et al. 2013, ApJ, 778, 96